


Layer-dependent electronic structure, dynamic stability, and phonon properties of few-layer SnSeFeng-ning Xue,¹ Zhi-hao Zhao,¹ Yujuan Zhang,² Ting Liu,¹ Yong Lu^{1b},^{1,*} and Ji-cai Zhang^{1,†}¹College of Mathematics and Physics, Beijing University of Chemical Technology, Beijing 100029, People's Republic of China²Institute of Nuclear Materials, School of Materials Science and Engineering, University of Science and Technology Beijing, Beijing 100083, People's Republic of China (Received 5 April 2022; revised 22 August 2022; accepted 24 August 2022; published 1 September 2022)

There is still a lack of fundamental understanding of the structural properties and thermal conductivity of few-layer SnSe, although it is the current recording material for thermoelectric conversion efficiency. From first-principles molecular dynamics and lattice dynamics, the electronic structure, structural properties, and lattice vibrational properties of few-layer SnSe are thus investigated in this study. The results show that SnSe exhibits semiconducting characteristics with the optical absorption mainly concentrated in the visible and near-ultraviolet regions. The band gap varies from 0.90 to 1.35 eV as the number of atomic layers decreases from bulk to single layer (1L). Four-layer (4L) SnSe shows typical bulk characteristics in terms of phase stability and electronic and vibrational properties. On further reducing the number of atomic layers, the quantum confinement effect becomes significant. At room temperature, the *Pnma* structural symmetry of 4L SnSe is dominated by the Jahn-Teller effect, consistent with the bulk phase. The second-order phase transition from *Pnma* to *Cmcm* driven by the phonon anharmonic effect occurs in 1L SnSe. A competitive picture of these two effects can be observed in 3L and 2L SnSe. At the enhancement temperature, the distribution peak of the phonon density of states between 3.5 and 4.5 THz shows a significant redshift relative to the harmonic case, exhibiting strong phonon anharmonicity. Correspondingly, the Raman-active normal modes B_{3g}^1 and A_g^2 , which contribute to the peak, present significant frequency softening, consistent with the experimental observations. The reduction in the number of atomic layers will aggravate the frequency softening of these modes. Due to the strong phonon anharmonicity and dynamic instability of the *Pnma* phase, the lattice thermal conductivity of few-layer SnSe at room temperature is significantly lower than that of the bulk phase.

DOI: [10.1103/PhysRevB.106.104301](https://doi.org/10.1103/PhysRevB.106.104301)**I. INTRODUCTION**

Due to their physical behavior, IV-VI semiconductors have aroused great interest in next-generation optoelectronic, thermoelectric, and photovoltaic devices [1–7]. As an important member of this family, SnSe compounds exhibit superior thermoelectric properties in the medium-temperature region, holding promise for thermoelectric and photovoltaic technologies [8,9]. Bulk SnSe crystallizes in an orthogonal layered structure and experiences a second-order displacement phase transition from *Pnma* to *Cmcm* above 600 K. The high-temperature *Cmcm* phase shows a much higher figure of merit than the low-temperature *Pnma* phase, which is mainly attributed to the enhanced coupling of phonon anharmonicity and high band degeneracy [8–10].

The out-of-plane layered structure with van der Waals interactions facilitates the experimental preparation of SnSe flakes or the exfoliation of single-layer SnSe from the bulk phase. Experimentally, single-crystal SnSe nanosheets with four atomic layers (1 nm) were first synthesized by the one-pot synthesis method [11]. The fabrication of SnSe thin films has been offered as an effective way to improve thermo-

electric and photoelectric properties. For example, a hybrid photodetector based on SnSe nanosheets with a thickness of 1 nm has a response time of 0.19 s. Compared with the three-dimensional SnSe nanoflower hybrid photodetector with a response time of 11.76 s, the SnSe nanosheets exhibit superior charge dissociation and transmission due to the two-dimensional (2D) properties [11]. Similarly, Zhao *et al.* [12] synthesized single-crystal orthorhombic SnSe nanoplates of different sizes with controllable side lengths from 1 to 6 μm by vapor transport deposition, showing a high photoresponsivity of 0.06 μA under a bias of 0.1 V. Ju and Kim [13] fabricated SnSe nanosheet composites, which show extremely low thermal conductivity and significant improvement in power factor. Ren *et al.* [14] prepared 2D SnSe nanosheets via a simple hydrothermal intercalation and exfoliation route. Photoelectrochemical tests demonstrated that the photocurrent density of SnSe nanosheets is greatly improved compared with the bulk phase. Recently, the rectangular SnSe flakes were reported to grow with a thickness of $6.8 \pm 1.4 \text{ \AA}$, which is close to the value of a single-layer SnSe (5.749 \AA) [15]. These nanostructures are of great significance for the manufacture of devices due to their low dimensions and relatively high performance.

Significant developments in the fabrication and manipulation of ultrathin SnSe films have also prompted theoretical studies of multilayer SnSe focusing on the electronic

*Corresponding author. luy@mail.buct.edu.cn†Corresponding author. jczhang@mail.buct.edu.cn

structure, heat transport behavior, doping, and strain effects [16–20]. In particular, since the number of scattering centers decreases as the thickness of SnSe flakes reduces to a level close to the single layer, the intensity of the Raman signal vanishes due to the limitation of the Raman spectrometer [15,21]. Clarifying the electronic, structural, and vibrational properties of these ultrathin films is crucial for device application. Although there has been much research on and understanding of the electronic properties of few-layer SnSe, less is known about its structural properties and lattice thermal conductivity. In particular, 2D SnSe has different properties than the bulk phase in terms of surface and boundary effects and quantum size effect. With the decrease in the number of atomic layers, there is still a lack of sufficient understanding of the competing relationship between the bulk and the two-dimensional characteristics of structural stability and vibrational properties of SnSe, which is an obvious obstacle to its application. Therefore, in this study, we will use the advantages of theoretical methods to study the microscopic quantum properties, mainly focusing on the layer-dependent structural properties, dynamic stability, and lattice thermal conductivity of few-layer SnSe. The phonon quasiparticle approach based on first-principles molecular dynamics (MD) simulations is used to deal with the anharmonic phonon properties [22,23], which is fundamentally different from the most commonly used density functional theory (DFT) phonon-based methods that use third-order force constants calculated from the static structure at 0 K. In this approach, temperature-dependent phonon frequencies and lifetimes are extracted from the phonon power spectrum calculated using the velocity autocorrelation function, thereby implying thermal effects and anharmonicities. Since the heat transport and optical properties have great significance for the characterization of materials, we also predict the lattice thermal conductivity and the optical absorption spectra of these compounds. Then the competing relationship between the properties of the bulk and 2D phases is revealed with the decrease of the number of atomic layers. It is expected that these results can provide an important theoretical reference for experimental verification and device application of SnSe.

II. METHODS AND COMPUTATIONAL DETAILS

The first-principles total energy and electronic structure calculations were carried out using density functional theory with the projector augmented-wave method [24] as implemented in the VASP package [25–27]. The electron exchange and correlation potential was described by the generalized gradient approximation parametrized by Perdew, Burke, and Ernzerhof [28]. The plane-wave cutoff was set to 300 eV. A Monkhorst-Pack $8 \times 8 \times 1$ mesh was used in Brillouin zone integration [29], which is sufficient to converge the results to less than 1.0×10^{-4} eV/atom. In order to correct the underestimation of the semiconductor band gap in DFT calculations based on the Kohn-Sham equations, the DFT-1/2 self-energy correction method was employed [30], which adds a self-energy correction to the standard potential. This approach differs from the Heyd-Scuseria-Ernzerhof (HSE06) approach commonly used in previous studies [31–33]. It is inspired by the simple half-ionization method, which reliably

describes the excited states in solids, giving band-gap energies and band structures in very good agreement with experiment. The harmonic second-order interatomic force constant matrix was calculated using a $4 \times 4 \times 1$ supercell and the finite displacement method with a displacement amplitude of 0.01 Å for bulk and few-layer SnSe. Then the harmonic phonon frequencies and polarization vectors were obtained with the postprocessing software PHONOPY [34].

All the first-principles MD simulations were performed using the $4 \times 4 \times 1$ supercell at 300 K. Only the Γ point is considered in the Brillouin zone integration. The canonical ensemble (NVT) was used and the temperature oscillations during the simulation were controlled by the Nosé thermostat [35]. The simulation time was 60 ps for each MD run with a 2 fs time step.

The phonon quasiparticle is defined by the power spectrum projected on the normal mode (\mathbf{q}, s) [22,23]

$$G_{\mathbf{q},s}(\omega) = \int_0^\infty \langle \mathbf{V}(0) \cdot \mathbf{V}(t) \rangle_{\mathbf{q},s} e^{i\omega t} dt. \quad (1)$$

For a normal mode, its typical power spectrum follows a Lorentzian-type line shape, from which both the quasiparticle frequency $\tilde{\omega}_{\mathbf{q},s}$ and linewidth $\Gamma_{\mathbf{q},s}$ can be extracted. The velocity autocorrelation function (VAF) in Eq. (1) can be calculated as

$$\langle \mathbf{V}(0) \cdot \mathbf{V}(t) \rangle_{\mathbf{q},s} = \lim_{t_0 \rightarrow \infty} \frac{1}{t_0} \int_0^{t_0} \mathbf{V}_{\mathbf{q},s}(t') \mathbf{V}_{\mathbf{q},s}(t'+t) dt', \quad (2)$$

in which the mode-projected velocity of the normal mode (\mathbf{q}, s) is

$$\mathbf{V}_{\mathbf{q},s}(t) = \sum_{i=1}^N \mathbf{V}(t) e^{-i\mathbf{q} \cdot \mathbf{R}_i} \cdot \hat{\mathbf{e}}_{\mathbf{q},s}. \quad (3)$$

$\mathbf{V}(t) = \{v_1(t)\sqrt{M_1}, \dots, v_N(t)\sqrt{M_N}\}$ is the mass-weighted velocity containing $3N$ components, and $v_i(t)$ ($i = 1, \dots, N$) are atomic velocities obtained from the first-principles MD simulation with N atoms per supercell. M_i and \mathbf{R}_i are the atomic mass and coordinates of atom i in the supercell. $\hat{\mathbf{e}}_{\mathbf{q},s}$ is the polarization vector of the harmonic phonon mode (\mathbf{q}, s) .

The lattice thermal conductivity κ_{lat} based on the Boltzmann transport equation and phonon gas model can be calculated as [36]

$$\kappa_{\text{lat}}^{\alpha\beta} = \sum_{\mathbf{q},s} C_v(\mathbf{q},s) v_{\mathbf{q},s}^\alpha v_{\mathbf{q},s}^\beta \tau_{\mathbf{q},s}, \quad (4)$$

where $v_{\mathbf{q},s}^{\alpha(\beta)}$ is the group velocity component along the α (β) direction and $\tau_{\mathbf{q},s}$ is the phonon lifetime of mode (\mathbf{q}, s) . $C_v(\mathbf{q}, s)$ is the mode-specific capacity of the expression,

$$C_v(\mathbf{q}, s) = \frac{k_B}{N\Omega} \left(\frac{\hbar\omega}{k_B T} \right)^2 f_0(f_0 + 1), \quad (5)$$

where k_B is the Boltzmann constant, \hbar is the reduced Planck constant, $\omega_{\mathbf{q},s}$ is the phonon frequency, N is the number of \mathbf{q} points, Ω is the volume of the unit cell, and f_0 is the Bose-Einstein statistics.

According to the dielectric theory, the optical properties were determined by the complex dielectric function $\varepsilon(\omega)$, which can be calculated by the independent particle approximation as implemented in VASP [37]. The dielectric function

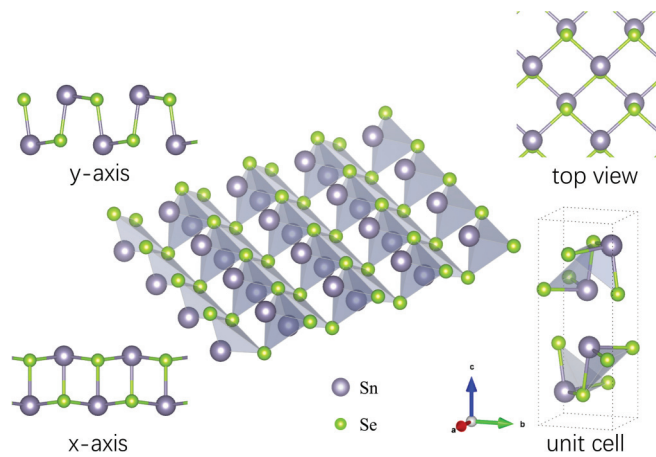


FIG. 1. The crystal structure of bulk SnSe in the $Pnma$ phase and the stripped single-layer SnSe along the out-of-plane direction. Atomic structures for different crystal directions are provided, namely, the x axis (zigzag direction), the y axis (armchair direction), and a top view.

gives the linear response of an electronic system submitted to an applied external electric field and can be written as $\varepsilon(\omega) = \varepsilon_1(\omega) + i\varepsilon_2(\omega)$. The imaginary part of the dielectric function is obtained from the momentum matrix elements between the occupied and unoccupied wave functions within the selection rules and is given by [38,39]

$$\varepsilon_2(\omega) = \frac{2e^2\pi}{\Omega\varepsilon_0} \sum |\langle \psi_k^c | \hat{u} \times r | \psi_k^v \rangle|^2 \delta(E_k^c - E_k^v - E), \quad (6)$$

where Ω is the unit cell volume and ψ_k^c and ψ_k^v are the conduction band and valence band wave functions at k , respectively. The real part of the dielectric function follows from the Kramers-Kronig relationship [40]. The absorption coefficient $\alpha(\omega)$ can be derived from $\varepsilon_1(\omega)$ and $\varepsilon_2(\omega)$ according to the following equation [41]:

$$\alpha(\omega) = \frac{\sqrt{2}\omega}{c} \left[\sqrt{\varepsilon_1^2(\omega) + \varepsilon_2^2(\omega)} - \varepsilon_1(\omega) \right]^{\frac{1}{2}}, \quad (7)$$

where c is the vacuum speed of light.

TABLE I. Optimized lattice constants (\AA) and energy band gaps E_g (eV) for bulk and few-layer SnSe. Experimental results in Ref. [11] and previous theoretical results [31–33,43] are also listed for comparison. The energy band gaps of Ref. [43] were calculated using the DFT method with a scissor of 0.5 eV. Data from Refs. [31–33] were calculated using the hybrid HSE06 functional method.

Type	a (\AA)	b (\AA)	b/a	E_g (eV)	E_g (eV) [11,31–33,43]
Bulk	4.150 ^a	4.450 ^a	1.072 ^a		0.90 ^a
Bulk	4.219	4.524	1.072	0.90	0.93 ^b , 0.86 ^c , 1.12 ^d , 1.00 ^e
4L	4.221	4.511	1.069	0.92	
3L	4.237	4.486	1.059	0.99	1.10 ^c
2L	4.241	4.479	1.056	1.08	1.15 ^b , 1.39 ^d , 1.20 ^e
1L	4.287	4.385	1.023	1.35	1.79 ^b , 1.32 ^c , 1.43 ^d , 1.44 ^e

^aReference [11].

^bReference [43].

^cReference [31].

^dReference [32].

^eReference [33].

III. RESULTS AND DISCUSSION

A. Atomic and electronic structures

The atomic structures of layered SnSe are shown in Fig. 1. Bulk SnSe crystallizes in the orthorhombic structure of space group $Pnma$ (No. 62) [36]. The few- or single-layer SnSe can be directly stripped from the bulk phase along the normal direction (c axis) due to the weak van der Waals interaction between the layers. SnSe structures with atomic layer thicknesses ranging from four layers (4L) to a single layer (1L) are considered in the present study and have the $P2_1/m$ (No. 11) phase for 4L and 2L SnSe and the $Pmn2_1$ (No. 31) phase for 3L and 1L SnSe. The optimized lattice parameters a (zigzag direction) and b (armchair direction) are summarized in Table I. For the bulk phase, the lattice constants a and b are 4.219 and 4.524 \AA , respectively, in agreement with experimental values of 4.15 and 4.45 \AA [8,11]. The lattice parameters of 4.221 and 4.511 \AA for 4L SnSe are very close to the values of the bulk phase. As the number of atomic layers decreases from 4L to 1L, the lattice parameters along the zigzag direction a and the armchair direction b increase and decrease, respectively. As listed in Table I, the b/a ratio decreases from 1.069 to 1.032, indicating that the anisotropy between the lattice parameters is reduced with the decrease in the number of atomic layers.

The orbital-resolved electronic density of states (DOS) of the few-layer SnSe were calculated and are shown in Fig. 2. We have tested the effect of van der Waals interactions on the electronic structure of bulk and few-layer SnSe using the optimized Becke88 van der Waals (optB88-vdW) method [44]. The calculated DOSs without and with van der Waals interactions are compared in Fig. S1 in the Supplemental Material, and the valence band maximum (VBM) levels, conduction band minimum (CBM) levels, and band gaps are collected in Table S1 [42]. The van der Waals interactions are found to have little effect on the electronic structure of bulk and few-layer SnSe, including energy levels at the VBM and CBM, electron orbital occupancy, and energy band gap. Therefore, in the following studies, we did not include van der Waals interactions. All these compounds show semiconductor characteristics with a considerable band gap. Detailed band structure calculations indicate that these compounds are

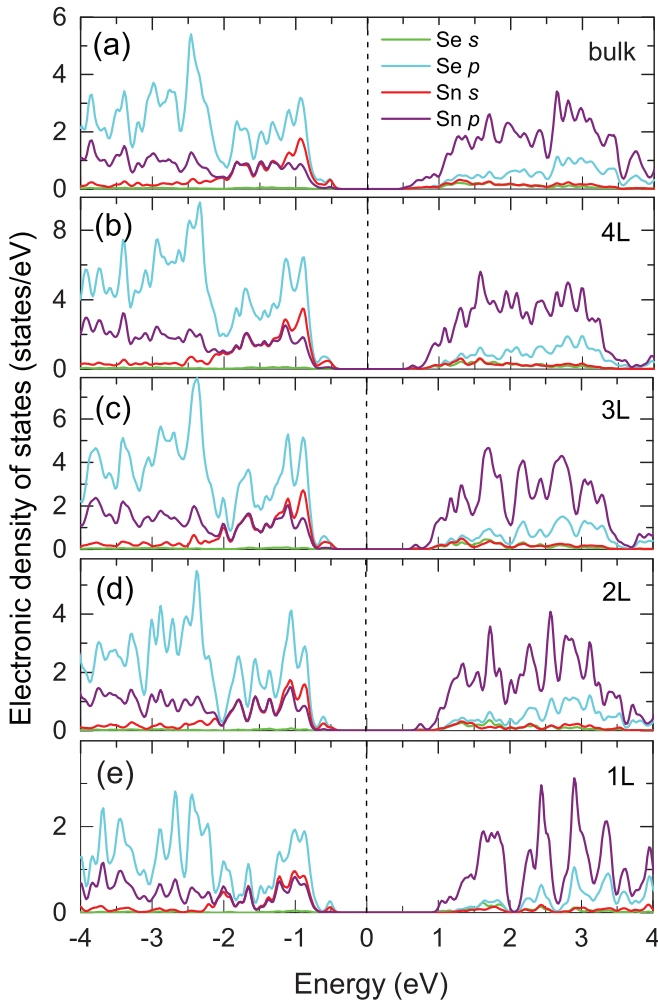


FIG. 2. The orbital-resolved electronic density of states (DOS) of bulk and few-layer (4L to 1L) SnSe. The Fermi level is set to zero.

indirect semiconductors (see Fig. S2 in the Supplemental Material) [42]. The VBM and the CBM appear in the Γ - Y and Γ - X directions, respectively, in agreement with previous reports [31–33,43]. For the bulk phase, the predicted band gap of 0.90 eV from the DFT-1/2 approach is in accordance with the experimental value of 0.90 eV [11]. The valence and conduction bands are significantly composed of the Se p orbital and the Sn p orbital, respectively. High hybridization between the Se p orbital and the Sn s orbital can be observed near the VBM. The electronic DOS distribution of the 4L SnSe is similar to that of the bulk phase with a very close band gap of 0.92 eV. As the number of atomic layers decreases, the contribution of the Sn s orbital to the Sn-Se bond near the VBM becomes weaker. Then, the 2D quantum confinement effect becomes significant, which is manifested in a more discrete peak distribution of the DOS. This is particularly true in 1L SnSe with an enlarged band gap of 1.35 eV. As shown in Table I, the band gap predicted by the DFT-1/2 method is consistent with the previous results calculated by the HSE06 approach [31–33], which presents an increasing trend with the decrease in the number of atomic layers. In addition, the Bader effective charges are +1.888 for Sn and -8.109 for Se in the 4L phase, very close to the values of +1.881 and -8.119 for

the bulk phase. As the number of atomic layers decreases, the Bader charges increase to +1.893 for Sn and -8.100 for Se in the 1L phase, indicating the reduced ionicity of the Sn-Se bond.

B. Dynamic stability at finite temperature

First-principles MD simulations were performed to elucidate the structural stability of few-layer SnSe at 300 K. Figure 3 shows the calculated atomic displacement probability distribution functions of Sn and Se atoms projected on the xy plane (in plane). For 4L SnSe, all Sn and Se atoms vibrate around the equilibrium lattice point with the probability distribution function showing only one main peak, as shown in Figs. 3(a)–3(d). Relative to the ideal $Pnma$ structure, the maximum appears at zero displacement, indicating phase stabilization. The $Pnma$ phase of bulk SnSe is known to be more energetically stable at low temperature than the $Cmcm$ phase. This is mainly due to the Jahn-Teller effect, which leads to a boost in state degradation by breaking the symmetry of the structure [10]. At high temperature, the phonon anharmonic effect becomes more important than the Jahn-Teller effect, promoting the stability of the high-symmetry $Cmcm$ phase. It can be seen that 4L SnSe exhibits the same characteristics as the bulk phase not only in terms of electronic structure but also in terms of phase stability. However, in the 1L SnSe, the vibrations of all atoms deviate from the equilibrium position. As shown in Figs. 3(m)–3(p), Sn and Se atoms tend to move opposite each other along the y axis (armchair direction). This corresponds to a second-order displacive phase transition from the $Pnma$ to $Cmcm$ phase, consistent with previous theoretical findings [36]. Unlike the bulk phase, the atomic structure is not limited by the Jahn-Teller effect in 1L SnSe, but the phonon anharmonic effect plays a major role in the phase transition. Deviations from the equilibrium position can also be observed in 2L and 3L SnSe, as shown in Figs. 3(e)–3(l). Unlike in 1L SnSe, Sn and Se atoms do not move along a direct phase transition path from the $Pnma$ phase to the $Cmcm$ phase but move along the x and y axes simultaneously. The instability of the $Pnma$ phase should be attributed to the coupling of the Jahn-Teller effect to the phonon anharmonicity in 2L and 3L SnSe.

To evaluate the phonon anharmonicity in SnSe, the phonon DOS at 300 K were calculated from the Fourier transform of the atomic VAF, as shown in Fig. 4. Four typical peaks labeled P_1 , P_2 , P_3 , and P_4 are marked in Fig. 4(a), the frequencies of which are distributed from low to high. Typical peaks in the phonon DOSs are contributed by different phonon vibrational modes. We identify these typical peaks, namely, P_1 – P_4 , by combining the phonon frequencies and the polarization vectors of the typical normal modes. At 0 K, the peak positions of P_1 to P_4 are located at 2.21, 3.76, 4.48, and 5.22 THz, respectively, in bulk SnSe. When the temperature increases to 300 K, the change in the low-frequency P_1 peak is subtle. The phonon anharmonicity is mainly reflected in the intermediate-frequency and high-frequency regions. The P_2 and P_3 peaks in the intermediate-frequency region show a significant redshift, the frequencies of which decrease by 0.27 and 0.15 THz, respectively. The distinct high-frequency P_4 peak disappears with increasing temperature. Instead, the phonon DOS in this

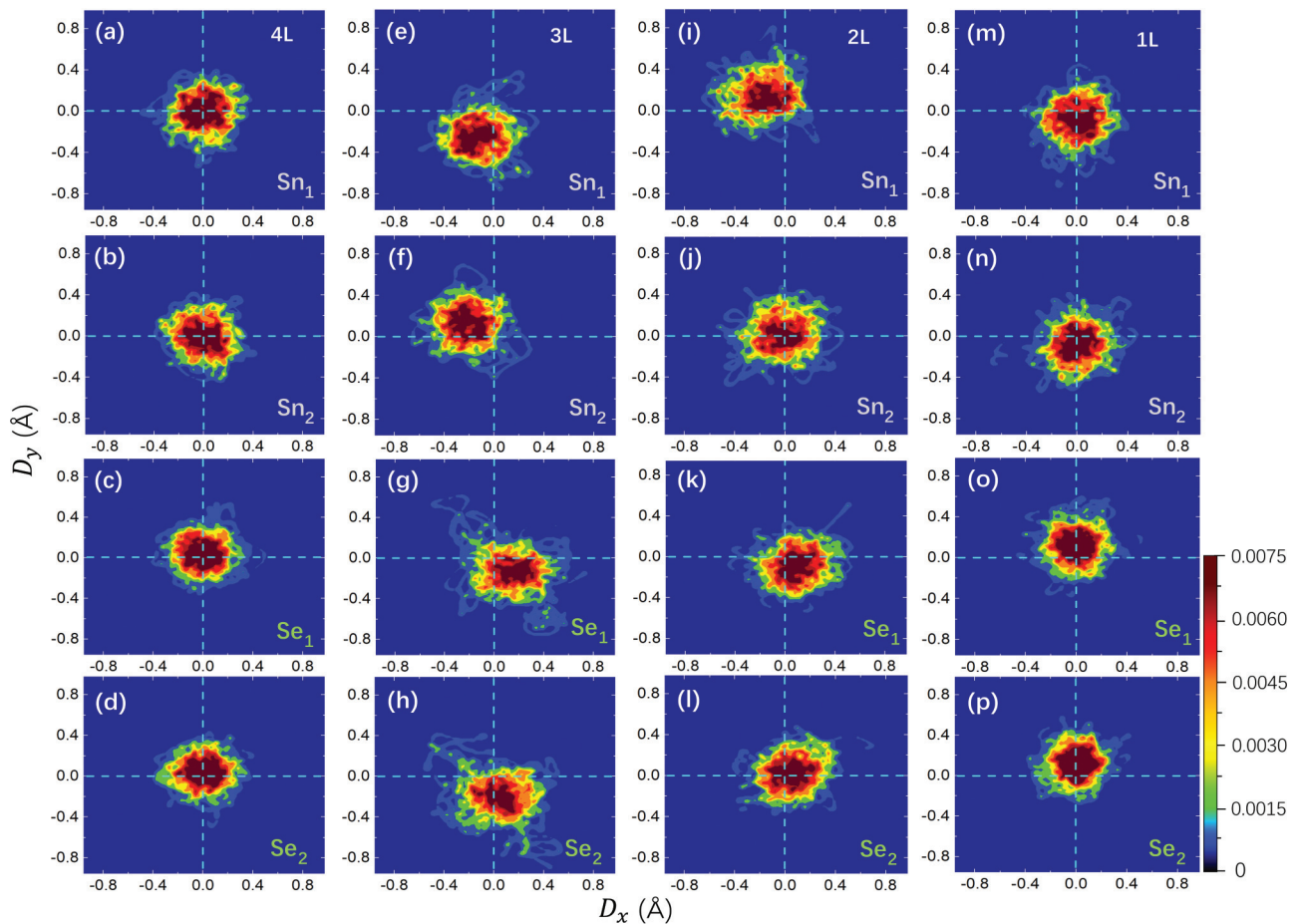


FIG. 3. Probability distribution function of atomic displacements projected onto the xy plane relative to the ideal $Pnma$ phase at 300 K. Distribution functions (a)–(d) for 4L SnSe, (e)–(h) for 3L SnSe, (i)–(l) for 2L SnSe, and (m)–(p) for 1L SnSe. The subscripts 1 and 2 stand for Sn or Se atoms on the lower and upper surfaces of the layered SnSe. The color scale represents the distribution probability (%).

region becomes flatter compared to the harmonic case. In 4L SnSe, the positions of the P_1 , P_2 , and P_3 peaks change little compared to the bulk phase. The main difference is that the P_4 peak does not disappear at the enhancement temperature, the position of which is lowered by 0.12 THz. With a further reduction of the layer thickness, the P_1 , P_2 , and P_3 peaks show significant layer dependence. The P_1 and P_3 peaks present a clear blueshift, while the P_2 peak shows a redshift. Especially in 1L SnSe, the changes in the P_2 and P_3 peaks are more pronounced. The position of the P_2 peak is 0.70 THz lower than in the bulk phase. In contrast, the position of the P_3 peak is greatly enhanced and incorporated into the P_4 peak. As a result, the effect of the phonon anharmonic effect on the P_4 peak in 1L SnSe is different from that in bulk and few-layer SnSe. That is, the position of the P_4 peak in 1L SnSe is shifted upwards at enhanced temperature, while in other few-layer SnSe it is shifted downwards.

The phonon power spectrum in reciprocal space was calculated according to Eq. (1) to reveal the layer-dependent behavior of specific normal modes at finite temperature. Since the bulk $Pnma$ SnSe belongs to the D_{2h} point group, the normal modes at the Γ point can be expressed as $\Gamma = [3B_{1u}(\text{IR}) + B_{2u}(\text{IR}) + 3B_{3u}(\text{IR}) + 4A_g(\text{R}) + 2B_{1g}(\text{R}) + 4B_{2g}(\text{R}) + 2B_{3g}(\text{R})]$ [45] according to the irreducible representation. IR and R represent the infrared-active

and Raman-active vibrational modes, respectively. Based on group theory, there are 12 Raman-active modes, all of which are even-parity optical phonon modes with inversion symmetry. The calculated frequencies of all Raman-active modes are listed in Table II. There are also seven IR activation modes, the frequencies of which are listed in the Supplemental Material in Table S2 [42] for comparison with experimental data [48]. In Figs. 5(b)–5(e), we depict the phonon power spectra of four typical Raman-active modes, A_g^1 , B_{3g}^1 , A_g^2 , and A_g^3 , which have been experimentally detected using a Raman spectrometer [31,46,47]. Compared with bulk SnSe, these few-layer structures have a lower group symmetry. Therefore, we identify these normal modes by combining the phonon frequency and polarization vector and label them uniformly using the same representation as the bulk phase. According to the polarization vector in Fig. 5(a), Raman modes A_g^1 and A_g^3 belong to the interlayer vibration modes, while B_{3g}^1 and A_g^2 belong to the in-plane vibration modes.

For a well-defined phonon quasiparticle, its power spectrum $G_{q,s}$ should have a Lorentzian-type line shape, from which the frequency and linewidth of each individual vibration mode can be unequivocally identified. At 300 K, all these phonon power spectra show a Lorentzian-type line shape with a single peak, indicating the validity of the phonon quasiparticle concept. The anharmonic phonon frequency $\omega_{q,s}$

TABLE II. The harmonic (0 K) and anharmonic (300 K) phonon frequencies (THz) of all Raman-active normal modes of bulk and few-layer SnSe. The experimental results of the A_g^0 , A_g^1 , B_{3g}^1 , A_g^2 , and A_g^3 modes from Refs. [31,46,47] are listed for comparison. Note that the harmonic experimental data were measured at 77 K.

Mode	T (K)	1L	2L	3L	4L	Bulk	Expt.
A_g^0	0		0.524	0.701	0.758	0.805	
	300		0.456	0.576	0.632	0.782	0.891 ^c
B_{3g}^0	0		0.915	0.744	0.973	0.811	
	300		0.960	0.580	0.906	0.820	
B_{2g}^0	0	1.360	1.454	1.680	1.267	1.342	
	300	1.352	1.398	1.660	1.242	1.534	
B_{2g}^1	0	1.380	1.481	1.690	1.526	1.781	
	300	1.144	1.462	1.588	1.450	1.826	
A_g^1	0	1.563	1.746	1.928	1.944	2.054	2.181 ^b
	300	1.694	1.728	1.874	1.960	2.080	2.085 ^a , 2.127 ^b , 2.025 ^c
B_{2g}^2	0	1.580	1.624	1.783	1.853	1.950	
	300	1.344	1.630	1.638	1.712	1.836	
B_{3g}^1	0	2.070	3.248	3.211	3.346	3.603	3.537 ^b
	300	1.712	2.614	2.674	2.752	3.430	3.270 ^a , 3.249 ^b
B_{1g}^0	0		2.567	3.404	3.665	3.667	
	300		2.210	3.314	3.444	3.622	
B_{1g}^1	0		3.188	3.629	3.749	3.757	
	300		2.522	3.506	3.274	3.522	
B_{2g}^3	0		3.424	3.669	4.090	4.020	
	300		3.432	3.134	3.828	3.874	
A_g^2	0	3.111	3.878	3.874	3.964	4.131	4.254 ^b
	300	2.982	3.542	3.632	3.540	3.960	3.918 ^a , 3.897 ^b , 3.921 ^c
A_g^3	0	4.779	4.545	4.558	4.542	4.348	4.614 ^b
	300	4.916	4.574	4.472	4.528	4.256	4.485 ^a , 4.520 ^b , 4.410 ^c

^aReference [31].

^bReference [46].

^cReference [47].

and lifetime $\tau_{q,s}$ can be obtained from the peak position and linewidth $\Gamma_{q,s}$ with the relationship $\tau_{q,s} = 1/(2\Gamma_{q,s})$, respectively. Phonon frequencies for these modes are gathered in Table II. Experimental results [31,46,47] and calculated harmonic data for bulk SnSe are also listed for comparison. Overall, the calculated harmonic frequencies of bulk SnSe are in agreement with the experimental results at 77 K, with a maximum error of less than 6% [46]. After accounting for temperature effects, the B_{3g}^1 , A_g^2 , and A_g^3 modes exhibit significant frequency softening, while the A_g^1 mode is insensitive to temperature in the bulk phase, consistent with experimental observations [31,46,47]. With the decrease in the number of atomic layers, these normal modes show clear layer dependence. Modes other than A_g^3 are significantly redshifted. This is particularly true for the B_{3g}^1 and A_g^2 modes in 1L SnSe, the frequencies of which drop significantly. This is consistent with the above phonon DOS results. Since the B_{3g}^1 and A_g^2 modes mainly contribute to the P_2 peak of the phonon DOS, it exhibits a notable redshift in 1L SnSe. On the contrary, the A_g^3 mode shows a blueshift a decrease in the number of atomic layers. The A_g^3 mode is an interlayer mode caused by the vibrations of two rigid layers relative to each other. This normal mode is involved in the P_4 peak of the phonon DOS, which is shifted by a substantial 0.66 THz in 1L SnSe relative to the bulk phase. As the number of atomic layers decreases from 4L to 1L, the linewidths of the A_g^1 and B_{3g}^1 modes are

significantly enhanced, indicating a decrease in the phonon lifetime of these two modes. Conversely, the lifetime of the A_g^2 and A_g^3 modes is slightly enhanced according to the decreased linewidth in the 1L SnSe.

C. Heat transport and optical absorption properties

After obtaining the linewidth $\Gamma_{q,s}$ from the power spectrum $G_{q,s}$, the phonon lifetime $\tau_{q,s}$ is then obtained with the relationship $\tau_{q,s} = 1/(2\Gamma_{q,s})$, as shown in Fig. S3 in the Supplemental Material [42], which can be used to calculate the lattice thermal conductivity κ_{lat} according to Peierls-Boltzmann theory [49,50]. κ_{lat} of few-layer SnSe is calculated using the anharmonic phonon frequency and phonon lifetime based on the phonon quasiparticle method according to Eq. (4). For 4L SnSe, a large anisotropy of κ_{lat} is observed along the zigzag and armchair directions, as shown in Fig. 6(a). The κ_{lat} value of $0.65 \text{ W m}^{-1} \text{ K}^{-1}$ along the zigzag direction is much higher than that of $0.32 \text{ W m}^{-1} \text{ K}^{-1}$ along the armchair direction, which is attributed to the significant anisotropy of the phonon group velocity in the two directions, as shown in the Supplemental Material in Fig. S4 [42]. For both directions, the optical branch provides a major contribution to the lattice thermal conductivity with respect to the acoustic branch. In 3L and 2L SnSe, the κ_{lat} values in the zigzag direction decrease to 0.46 and $0.45 \text{ W m}^{-1} \text{ K}^{-1}$, respectively. Along the armchair direction, the κ_{lat} values

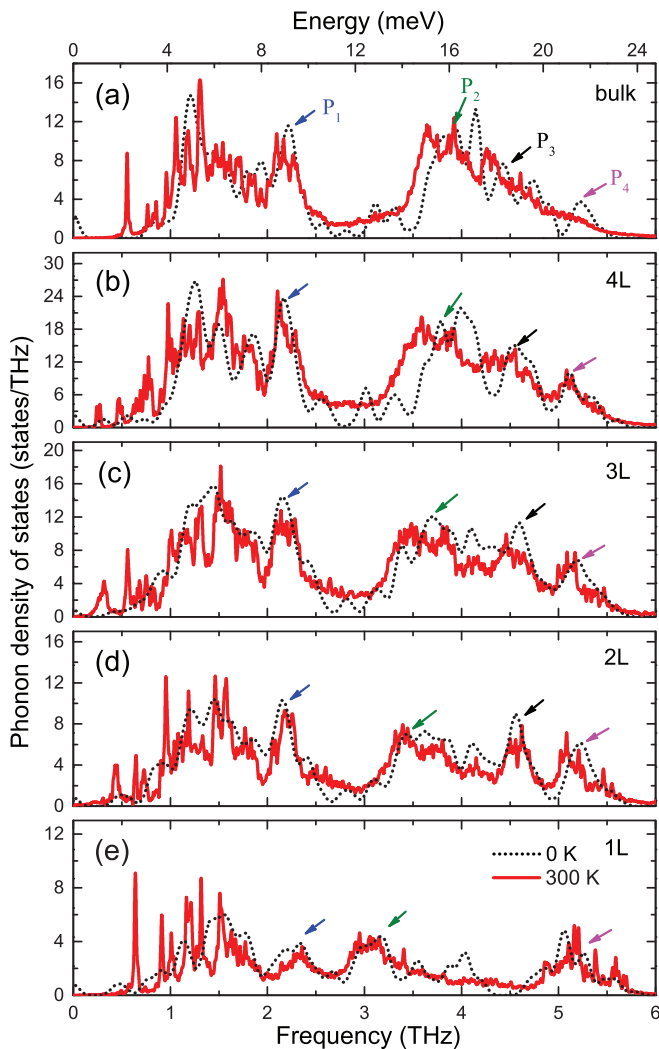


FIG. 4. The calculated phonon density of states of bulk and few-layer (4L to 1L) SnSe at 0 and 300 K.

increase by 0.06 and 0.04 $\text{W m}^{-1} \text{K}^{-1}$, respectively, mainly attributed to the increased contribution of the acoustic phonon modes. In 1L SnSe, the κ_{lat} value increases in both directions. The contribution of the acoustic branch to thermal conductivity becomes equivalent to that of the optical branch. The increase in the acoustic mode intensity mainly comes from the contribution of the first transverse acoustic (TA_1) mode, the lifetime of which increases significantly with decreasing the number of atomic layers, as shown in Fig. 6(b). Compared with the experimental values for the bulk phase, the thermal conductivity of few-layer SnSe decreases. Especially for 3L and 2L SnSe, the thermal conductivity decreases by nearly half along the armchair direction. This is attributed to the instability of the electronic structure, which increases the phonon anharmonicity in 3L and 2L SnSe. The Jahn-Teller effect tends to stabilize the low-symmetry $Pnma$ phase by breaking structural symmetry, whereas the phonon anharmonicity prefers the high-symmetry $Cmcm$ phase. A delicate competition between the two effects exists in 3L and 2L SnSe at room temperature, resulting in the instability of the $Pnma$ phase. In 3L and 2L SnSe, the vibration amplitudes of atoms

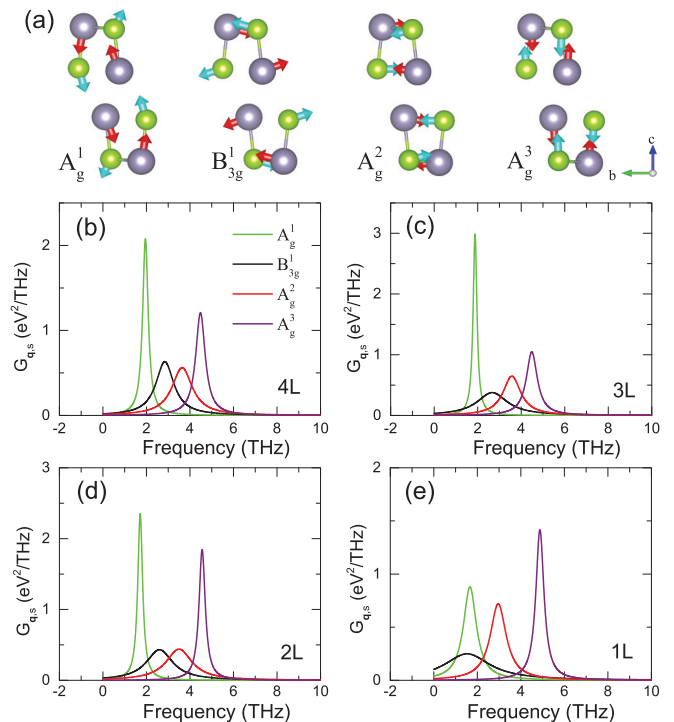


FIG. 5. Phonon polarization eigenvectors and power spectrum $G_{q,s}$ of the Raman-active normal modes A_g^1 , B_{3g}^1 , A_g^2 , and A_g^3 at the point $\mathbf{q} = \Gamma(0, 0, 0)$. The calculation temperature is 300 K. Phonon polarization eigenvectors are marked by colored arrows in (a).

away from the equilibrium position are larger than those in 4L and 1L SnSe, which would give rise to stronger lattice anharmonicity.

Optical properties are highly dependent on the electronic structure, which provide a feasible means to identify structural information and to characterize electronic structure through optical response of a material. The optical absorption coefficients $\alpha(\omega)$ of these compounds are calculated according to Eq. (7) and are shown in Fig. 7, where the visible regions are marked as shaded regions for convenience. The absorption region is mainly concentrated in the visible and near-ultraviolet

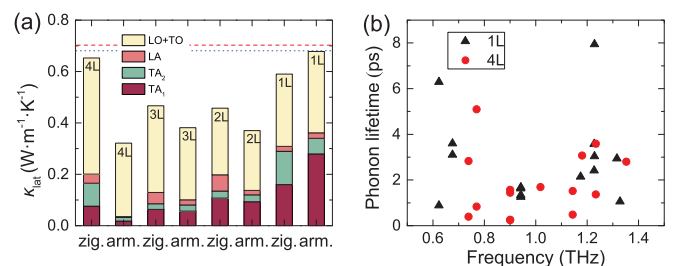


FIG. 6. (a) Lattice thermal conductivity of few-layer (4L to 1L) SnSe calculated along the zigzag and armchair directions. The contributions of the transverse acoustic branch (TA_1 and TA_2), longitudinal acoustic branch (LA), and optical branch (LO+TO) are indicated with different colors. Experimental results in Ref. [8] for the bulk SnSe are marked by the red dashed line (zigzag direction, zig.) and blue dotted line (armchair direction, arm.). (b) Phonon lifetimes of 1L and 4L SnSe as a function of frequency.

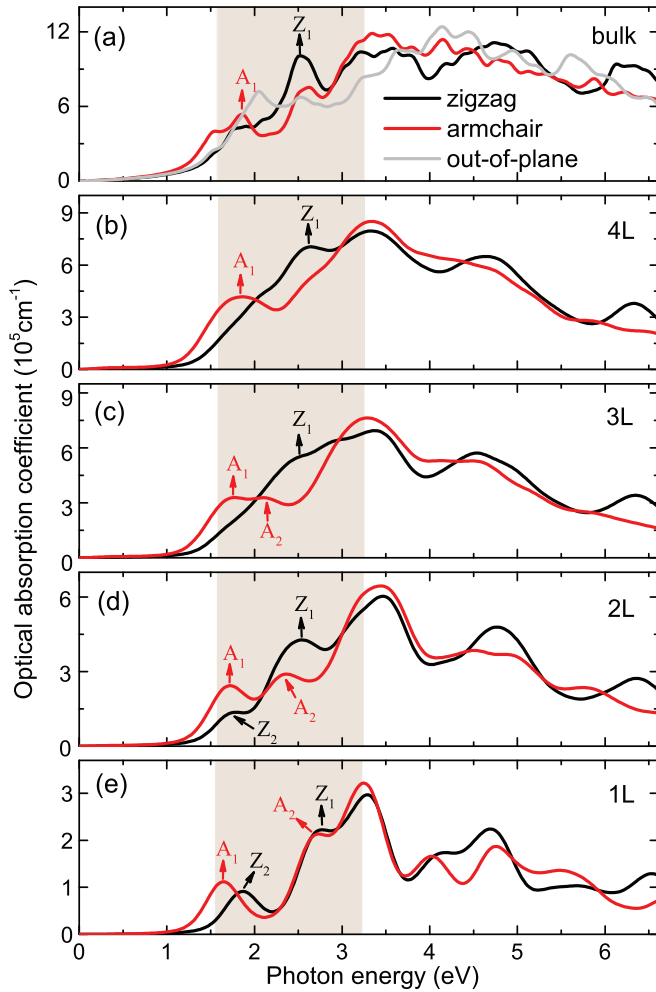


FIG. 7. Calculated optical absorption coefficients $\alpha(\omega)$ for bulk and few-layer (4L to 1L) SnSe. Visible light absorbing regions are shaded. A_x and Z_x ($x = 1, 2$) represent different absorption peaks along the armchair and zigzag directions in the visible region, respectively.

regions with absorption onsets in the infrared range for bulk and few-layer SnSe. After analyzing the electronic DOS in Fig. 2, this is mainly assigned to the contribution of electronic transitions from the Sn p orbital to the Se p orbital. The anisotropy of the optical absorption spectra along the zigzag and armchair directions is prominent in the bulk phase. A distinct absorption peak can be observed along the zigzag and armchair directions, which are located at 2.52 eV (labeled Z_1) and 1.87 eV (labeled A_1) in the visible region, respectively. The characteristics of 4L SnSe are similar to those of bulk SnSe, including the location and intensity of absorption peaks. Further reducing the number of atomic layers, the absorption curve in the visible region presents a multimodal distribution, which can be attributed to the enhanced quantum confinement effect. The A_1 peak is slightly redshifted with the decrease in the number of atomic layers. In 3L SnSe, a new absorption peak along the armchair direction (labeled A_2)

appeared at 2.15 eV, which was not observed in bulk and 4L SnSe. Reducing to the 2L SnSe, the A_2 peak is blueshifted to 2.32 eV. At the same time, another new absorption peak at 1.75 eV (labeled Z_2) appeared along the zigzag direction. After a further reduction to 1L SnSe, the A_2 and Z_2 peaks are further blueshifted to 2.71 and 1.86 eV, respectively. The A_2 and Z_2 peaks almost coincide. As a result, the anisotropy of the optical absorption spectrum along the zigzag and armchair directions is greatly weakened. Only the discrete A_2 and Z_2 peaks are clearly identifiable for the armchair and zigzag orientations.

IV. SUMMARY

In summary, we investigated the electronic and structural properties, phonon vibrational properties, and lattice thermal conductivity of few-layer SnSe through a combination of first-principles MD and lattice dynamics. The results indicate that the band gap increases from 0.90 to 1.35 eV as the number of atomic layers decreases from bulk to single layer, showing typical layer-dependent characteristics. From the electronic DOS, optical absorption spectrum, and phonon vibrational properties, 4L SnSe mainly shows characteristics of the bulk phase. The quantum confinement effect becomes significant when the number of atomic layers is lower than four. At room temperature, the Jahn-Teller effect and phonon anharmonicity play a major role in the phase stability of 4L and 1L SnSe, respectively. The competitive coupling between them exists in 3L and 2L SnSe, resulting in the instability of the $Pnma$ phase. Due to the phonon anharmonicity, the Raman-active normal modes B_{3g}^1 and A_g^2 show significant frequency softening in bulk and few-layer SnSe, in agreement with the experimental observations. With the decrease in the number of atomic layers, the two modes show a significant redshift. Compared with the harmonic vibrations, the phonon anharmonic effect mainly originates from the frequency softening of the phonon modes between 3.5 and 4.5 THz, corresponding to the redshift of the characteristic peaks in the phonon DOS. The predicted lattice thermal conductivity of few-layer SnSe is significantly lower than that of the bulk phase at room temperature. This is particularly true for 2L and 3L SnSe due to the strong coupling of phonon anharmonicity and phase instability. These theoretical results show us a clearer physical picture of few-layer SnSe in terms of electronic, structural, and phonon properties, which are expected to provide valuable references for the precise design and fabrication of nanodevices.

ACKNOWLEDGMENTS

This work was supported by the National Natural Science Foundation of China under Grants No. 12074028, No. 61874007, and No. 52102152 and partly by Shandong Provincial Major Scientific and Technological Innovation Project No. 2019JZZY010209 and the Key-area research and development program of Guangdong Province, Grant No. 2020B010172001.

- [1] Z. Z. Luo, S. Q. Hao, S. T. Cai, T. P. Bailey, G. J. Tan, Y. B. Luo, I. Spanopoulos, C. Uher, C. Wolverton, V. P. Dravid, Q. Y. Yan, and M. G. Kanatzidis, *J. Am. Chem. Soc.* **141**, 6403 (2019).
- [2] F. Zhang, J. Qiu, H. Guo, L. Wu, B. Zhu, K. Zheng, H. Li, Z. Wang, X. Chen, and J. Yu, *Nanoscale* **13**, 15611 (2021).
- [3] Q. Tian, W. Zhang, Z. Qin, and G. Qin, *Nanoscale* **13**, 18032 (2021).
- [4] S. Chandra, R. Arora, U. V. Waghmare, and K. Biswas, *Chem. Sci.* **12**, 13074 (2021).
- [5] Q. Qu, B. Liu, H. Liu, J. Liang, J. Wang, D. Pan, and I. K. Sou, *Nanoscale* **13**, 18160 (2021).
- [6] S. Liu, Y. Chen, S. Yang, and C. Jiang, *Nano Res.* **15**, 1532 (2022).
- [7] H. Li, J. K. Liang, Q. D. Wang, F. B. Liu, G. Zhou, T. Qing, S. H. Zhang, and J. Lu, *Nano Res.* **15**, 2522 (2022).
- [8] L. D. Zhao, S. H. Lo, Y. S. Zhang, H. Sun, G. J. Tan, C. Uher, C. Wolverton, V. P. Dravid, and M. G. Kanatzidis, *Nature (London)* **508**, 373 (2014).
- [9] M. Yang, W. Gao, M. He, S. Zhang, Y. Huang, Z. Zheng, D. Luo, F. Wu, C. Xia, and J. Li, *Nanoscale* **13**, 15193 (2021).
- [10] Y. Lu, F.-W. Zheng, Y. Yang, P. Zhang, and D.-B. Zhang, *Phys. Rev. B* **100**, 054304 (2019).
- [11] L. Li, Z. Chen, Y. Hu, X. Wang, T. Zhang, W. Chen, and Q. Wang, *J. Am. Chem. Soc.* **135**, 1213 (2013).
- [12] S. Zhao, H. Wang, Y. Zhou, L. Liao, Y. Jiang, X. Yang, G. Chen, M. Lin, Y. Wang, and H. Peng, *Nano Res.* **8**, 288 (2015).
- [13] H. Ju and J. Kim, *ACS Nano* **10**, 5730 (2016).
- [14] X. H. Ren, X. Qi, Y. Z. Shen, G. H. Xu, J. Li, Z. Q. Li, Z. Y. Huang, and J. X. Zhong, *Mater. Sci. Eng., B* **214**, 46 (2016).
- [15] J. Z. Jiang, C. Wong, J. Zou, S. Li, Q. Wang, J. Chen, D. Qi, H. Wang, G. Eda, D. Chua, Y. Shi, W. Zhang, and A. Wee, *2D Mater.* **4**, 021026 (2017).
- [16] A. K. Singh and R. G. Hennig, *Appl. Phys. Lett.* **105**, 042103 (2014).
- [17] F. Q. Wang, S. H. Zhang, J. B. Yu, and Q. Wang, *Nanoscale* **7**, 15962 (2015).
- [18] Y. J. Sun, Z. G. Shuai, and D. Wang, *J. Phys. Chem. C* **123**, 12001 (2019).
- [19] J. T. Lu, L. S. Guo, G. Xiang, Y. Nie, and X. Zhang, *J. Electron. Mater.* **49**, 290 (2020).
- [20] M. Luo, Y. Xu, and Y. H. Shen, *Results Phys.* **17**, 103126 (2020).
- [21] T. F. Pei, L. H. Bao, R. S. Ma, S. R. Song, B. H. Ge, L. M. Wu, Z. Zhou, G. C. Wang, H. F. Yang, J. J. Li, C. Z. Gu, C. M. Shen, S. X. Du, and H. J. Gao, *Adv. Electron. Mater.* **2**, 1600292 (2016).
- [22] D. B. Zhang, T. Sun, and R. M. Wentzcovitch, *Phys. Rev. Lett.* **112**, 058501 (2014).
- [23] Y. Lu, T. Sun, P. Zhang, P. Zhang, D. B. Zhang, and R. M. Wentzcovitch, *Phys. Rev. Lett.* **118**, 145702 (2017).
- [24] P. E. Blöchl, *Phys. Rev. B* **50**, 17953 (1994).
- [25] G. Kresse and J. Furthmüller, *Comput. Mater. Sci.* **6**, 15 (1996).
- [26] G. Kresse and J. Furthmüller, *Phys. Rev. B* **54**, 11169 (1996).
- [27] G. Kresse and D. Joubert, *Phys. Rev. B* **59**, 1758 (1999).
- [28] J. P. Perdew, K. Burke, and M. Ernzerhof, *Phys. Rev. Lett.* **77**, 3865 (1996).
- [29] H. J. Monkhorst and J. D. Pack, *Phys. Rev. B* **13**, 5188 (1976).
- [30] L. G. Ferreira, M. Marques, and L. K. Teles, *Phys. Rev. B* **78**, 125116 (2008).
- [31] S. Yang, Y. Liu, M. Wu, L.-D. Zhao, Z. Lin, H.-C. Cheng, Y. Wang, C. Jiang, S.-H. Wei, L. Huang, Y. Huang, and X. Duan, *Nano Res.* **11**, 554 (2018).
- [32] Y. Ye, Y. Xian, J. Cai, K. Lu, Z. Liu, T. Shi, J. Du, Y. Leng, R. Wei, W. Wang, X. Liu, G. Bi, and J. Qiu, *Adv. Opt. Mater.* **7**, 1800579 (2019).
- [33] L. C. Gomes and A. Carvalho, *Phys. Rev. B* **92**, 085406 (2015).
- [34] A. Togo, L. Chaput, I. Tanaka, and G. Hug, *Phys. Rev. B* **81**, 174301 (2010).
- [35] A. Nosé, *J. Chem. Phys.* **81**, 511 (1984).
- [36] Y. Lu, F. W. Zheng, Y. Yang, P. Zhang, and D. B. Zhang, *Phys. Rev. B* **103**, 014304 (2021).
- [37] B. Adolph, J. Furthmüller, and F. Bechstedt, *Phys. Rev. B* **63**, 125108 (2001).
- [38] Q. J. Liu, Z. T. Liu, L. P. Feng, and H. Tian, *Solid State Sci.* **12**, 1748 (2010).
- [39] R. Saniz, L. H. Ye, T. Shishidou, and A. J. Freeman, *Phys. Rev. B* **74**, 014209 (2006).
- [40] B. Holm, R. Ahuja, Y. Yourdshahyan, B. Johansson, and B. I. Lundqvist, *Phys. Rev. B* **59**, 12777 (1999).
- [41] K. Huang, *Solid-State Physics* (Higher Education Press, Beijing, 1988).
- [42] See Supplemental Material at <http://link.aps.org/supplemental/10.1103/PhysRevB.106.104301> for more information on the calculation of the electronic density of states with vdW interactions, the orbital-resolved band structure, the frequency of IR-active normal modes, the phonon lifetime versus frequency, and the phonon group velocity versus frequency for few-layer SnSe.
- [43] Y. Huang, L. Li, Y.-H. Lin, and C.-W. Nan, *J. Phys. Chem. C* **121**, 17530 (2017).
- [44] J. Klimeš, D. R. Bowler, and A. Michaelides, *J. Phys.: Condens. Matter* **22**, 022201 (2010).
- [45] I. Efthimiopoulos, M. Berg, A. Bande, L. Puskar, E. Ritter, W. Xu, A. Marcelli, M. Ortolani, M. Harms, J. Müller, S. Speziale, M. Koch-Müller, Y. Liu, L. D. Zhao, and U. Schade, *Phys. Chem. Chem. Phys.* **21**, 8663 (2019).
- [46] F. Liu, P. Parajuli, R. Rao, P. C. Wei, A. Karunarathne, S. Bhattacharya, R. Podila, J. He, B. Maruyama, G. Priyadarshan, J. R. Gladden, Y. Y. Chen, and A. M. Rao, *Phys. Rev. B* **98**, 224309 (2018).
- [47] Y. Han, J. Yu, H. Zhang, F. Xu, K. Peng, X. Zhou, L. Qiao, O. V. Misochko, K. G. Nakamura, G. M. Vanacore, and J. Hu, *J. Phys. Chem. Lett.* **13**, 442 (2022).
- [48] H. R. Chandrasekhar, R. G. Humphreys, U. Zwick, and M. Cardona, *Phys. Rev. B* **15**, 2177 (1977).
- [49] A. J. C. Ladd, B. Moran, and W. G. Hoover, *Phys. Rev. B* **34**, 5058 (1986).
- [50] J. E. Turney, E. S. Landry, A. J. H. McGaughey, and C. H. Amon, *Phys. Rev. B* **79**, 064301 (2009).